Chromium(III)-substituted hydroxyapatite/silica sol–gel coating: towards novel green coating for corrosion protection of AA2024

Sherif Elbasuney[1,2] · Ibrahim Naeem[1] · Mohamed Mokhtar[1] · Mohamed Sheashea[1] · Mahmoud Zorainy[1] ·
Gharieb S. El-Sayyad [3,4,5] · Mohamed Gobara[1]

Abstract

A novel Cr-substituted hydroxyapatite (Cr-HA) nanoparticles were synthesized via continuous hydrothermal technique. Moreover, the synthesized material was embedded into a silica sol–gel matrix and applied on an AA2024 substrate to evaluate the corrosion inhibition efficiency of the coating. TEM and SEM micrographs confirmed the development of Cr-HA nanorods of 20 nm width and 6 μm length. XRD diffractograms demonstrated the evolution of a new crystalline structure; the XRD pattern was analyzed by Material Studio software which confirms the replacement of Ca^{2+} by Cr^{3+}. The EDX mapping revealed a uniform distribution of Ca and Cr ions within the Cr-HA crystal structure. The atomic ratio of Ca^{2+}: Cr^{3+} was reported to be 4:1 respectively. The Cr-HA nanoparticles were uniformly distributed in a silica sol–gel matrix and applied on an AA2024 substrate. The corrosion performance of the Cr-HA sol–gel coating composite was evaluated using Electrochemical Impedance Spectroscopy (EIS) in an aerated 3.5% NaCl solution and the results compared to those of neat silica sol–gel coating. Whereas pitting corrosion was also observed in the case of a neat sol–gel coated sample within 5 days of immersion, Cr-HA sol–gel coated AA2024 exhibited prolonged pitting resistance over 110 days with no sign of corrosion or delamination. The EIS data fitting suggested the formation of a protective layer that is responsible for the extended corrosion resistance of the Cr-HA-coated sample. The scratch test indicated that the Cr-HA nanocomposite coating might offer short-term self-healing properties in the 3.5% NaCl corrosive media.

✉ Gharieb S. El-Sayyad
Gharieb.Elsayyad@gu.edu.eg

✉ Mohamed Gobara
m_gobara@yahoo.com

1 Chemical Engineering Department, Military Technical College, Cairo, Egypt

2 Nanotechnology Research Centre, Military Technical College, Cairo, Egypt

3 Microbiology and Immunology Department, Faculty of Pharmacy, Ahram Canadian University, Sixth October City, Giza, Egypt

4 Microbiology and Immunology Department, Faculty of Pharmacy, Galala University, Galala, Suez, Egypt

5 Drug Radiation Research Department, National Centre for Radiation Research and Technology (NCRRT), Egyptian Atomic Energy Authority (EAEA), Cairo, Egypt

Graphical Abstract
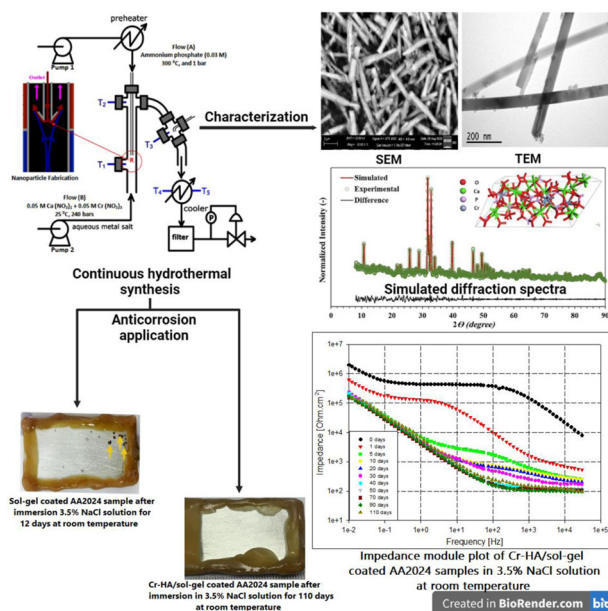
1 Introduction

Aluminum alloy AA2024 has been widely used in aviation applications for its high strength-to-weight ratio [1, 2]. Coating is an effective technique for corrosion protection. Various inhibitors have been incorporated into the coating matrix to enhance its corrosion resistance [3–7]. For many decades, chromate coatings were applied as a primary layer to improve the corrosion resistance of AA2024 [8]. However, the presence of hexavalent chromium in these coatings has been ruled out in the United States and Europe. Many researchers have endeavored to develop suitable replacements for Cr(VI) coatings [9–12]; sol–gel coatings could offer green alternatives [11, 13, 14]. Sol–gel coatings are easily synthesized to produce tailored coatings with desirable properties. These hybrid coatings comprise a combination of organic and inorganic segments in their chemical structure, which allow for modifying mechanical, physical, thermal, and chemical properties via adjusting the ratio between these two components. The most commonly used precursors for hybrid coatings are modified silicon alkoxides such as 3-glycidoxypropyl trimethoxysilane (GPTMS) [15, 16]. In addition, different solvents were applied in the synthesis of sol–gel coatings [17–19] to make them compatible with a wide range of additives. The sol–gel technique not only reduces the curing temperature but also, silica sol–gel coatings form a covalent bond (Si–O–Al) at the coating/metal interface [20, 21].

This strong bond improves the adhesion properties of the coating to the metal surface and enhances the barrier property against the diffusion of corrosive electrolyte via forming a three-dimensional siloxane network and consequently, increases the corrosion resistance [22]. Moreover, nanoparticle addition can enhance the mechanical properties of these coatings [23–25]. Last but not least, these coatings can accommodate different types of inhibitors elevating the corrosion-resistant properties of the silica sol–gel coated metals [13, 26–30].

Silica sol–gel coatings were loaded with hydroxyapatite (HA) as a corrosion inhibitor for AA2024 in artificial seawater [31]. HA is one of the most important materials used in medical, dental, drug delivery, water treatment, and materials science [32–35]. HA is a bio-compatible eco-friendly material constituting 70% of human bones. It is composed of calcium phosphate with the chemical formula $Ca_{10}(PO_4)_6(OH)_2$. HA can act as a buffering reagent stabilizing the pH of the corrosive medium and can also hinder the diffusion of corrosive species onto the metal surface. Consequently, HA potentially performs a dual function and therefore can provide remarkable durable protection.

The chemical structure of HA can be tailored for particular applications. In this regard, some selected metal ions can partially replace calcium ions within the HA matrix. For enhanced corrosion resistance, Cr(III) can confer HA advanced corrosion resistance properties. Continuous hydrothermal synthesis represents a facile approach for the sustainable fabrication of HA nanoparticles with controlled

morphology [36–38]. Furthermore, this ongoing technology can allow proper and controlled inclusion of different metal ions within the HA matrix [39]. Trivalent chromium coatings are considered a promising replacement for Cr (VI) coatings [1, 40–42]. Cr(III) coatings have been developed by the US military and have been unrestrictedly used as a benign substitution for hexavalent chromium coatings [43–45]. Although Cr(VI) traces were discovered in the Cr(III) treatments, the amount of Cr(VI) was insignificant (<0.1 wt.%) complying with the regulations of Registration, Evaluation, Authorization and Restriction of Chemicals [45]. In corrosion application, the main advantage of introducing Cr(III) into the HA crystal structure is to control interaction and extend the release of Cr within the sol–gel matrix; in addition, HA molecules assist the corrosion resistance properties of the silica sol–gel coatings [31, 46, 47].

This study reports the facile synthesis of Cr-substituted HA nanoparticles via a continuous hydrothermal process. Herein, up to our knowledge, it is the first time to partially replace Ca^{2+} with Cr^{3+} in the HA molecule via continuous hydrothermal synthesis. Novel high-quality mono-dispersed Cr-HA nano-rods of 20 nm width and 6 μm lengths were developed. The uniform dispersion of Cr within the HA matrix was verified via elemental mapping using EDAX analysis. Cr-HA experienced the evolution of a new crystalline structure. Material Studio software was also applied to confirm the replacement of the Ca atoms by Cr ones in the hydroxyapatite molecules. Moreover, the anti-corrosion properties of the prepared Cr-HA nanocomposite were examined. Cr-HA nanocomposite was dispersed in a silica sol–gel matrix forming a homogeneous coating. The advantage of using silica sol–gel with Cr-HA is that both components were dispersed in an aqueous alcoholic solution allowing the formation of a homogeneous matrix. The corrosion performance of the Cr-HA/sol–gel coating was evaluated as an active corrosion barrier to AA2024 in artificial seawater. The corrosion inhibition performance of Cr-HA containing sol–gel coating was assessed compared to neat silica sol–gel coating.

2 Materials and methods

2.1 Materials and sample preparation

Aluminum alloy AA2024-T3 (Q-panel™ incorporation, USA) was employed as the working electrode in corrosion experiments. The dimensions of the rectangular-shaped coupons were 12.5 cm, 2.5 cm, and 0.1 cm, respectively. The surface of the coupons was abraded using 320, 600, and 1200 grit silicon carbide (SiC), washed with ethanol, and subsequently rinsed in de-ionized water. Finally, the cleaned

coupons were dried at room temperature by a stream of compressed air for 1 min and stored in a desiccator till use.

2.2 Corrosive solution

A corrosive aqueous solution of 3.5 wt.% NaCl (NaCl purity ≥99.0%) was prepared to imitate the chloride-rich environment. It is the most widely utilized electrolyte in analogous investigations (e.g. ASTM G44 and G47) assessing the resistance of aluminum alloys. In such a harsh corrosive environment, the passive oxide layer formed on the aluminum surface undergoes deliberate damage and a localized corrosion attack takes place.

2.3 Synthesis of Cr-Hydroxyapatite

Hydrothermal processing offers a relatively straightforward route for nanoparticle fabrication whereby mono-dispersed nanoparticles of specific morphology can be easily developed by precisely controlling the synthesis conditions. Precursors for pristine HA synthesis included ammonium phosphate dibasic ($(NH_4)_2 HPO_4$; solution A) and calcium nitrate tetrahydrate ($Ca(NO_3)_2.4H_2O$; solution B). HA was fabricated via instantaneous mixing of 20 ml/min superheated stream of solution A (0.03 M, 300 °C and 1 bar) with 10 ml/min aqueous stream of solution B (0.1 M, 25 °C and 240 bars). The nanoparticles were continuously developed at the point where the two streams met inside the counter-current reactor (R) (Fig. 1).

On the other hand, Cr-HA nanoparticles were synthesized by partial replacement of Ca^{2+} with Cr^{3+}. Chromium(III) nitrate nonahydrate (99%, Aldrich) was employed as the precursor for Cr-substituted HA. The synthesis strategy included the use of a mixed solution for stream B consisting of 0.05 M calcium nitrate tetrahydrate and 0.05 M chromium(III) nitrate nonahydrate.

2.4 Preparation of Cr-HA/Sol–gel coating

Neat Silica sol–gel coating was prepared according to our previous method through acid-catalyzed hydrolysis followed by condensation using epoxy (450–500 g/equiv., ISEPAC, Egypt) and GPTMS (aka GLYMO, Sigma Aldrich, USA) as precursors [48]. The molar mixing ratio of GPTMS, epoxy, and acetone was set to 0.09: 0.02: 5.0, respectively. The prepared mixture was stirred at 60 °C till the formation of a clear mixture, which was cooled down to room temperature. To cure the solution, 3-aminopropyl triethoxysilicate (APTES) and diethylenetriamine (DETA) (Sigma Aldrich, USA) were then added at a molar ratio of 1:1 with respect to each other and with an overall molar ratio of 0.4:1 to the GPTMS-epoxy mixture. After adding the curing agents, the mixture was mechanically stirred for 6 h to ensure complete curing.

Fig. 1 Schematic for continuous hydrothermal synthesis of Cr-HA nanocomposite
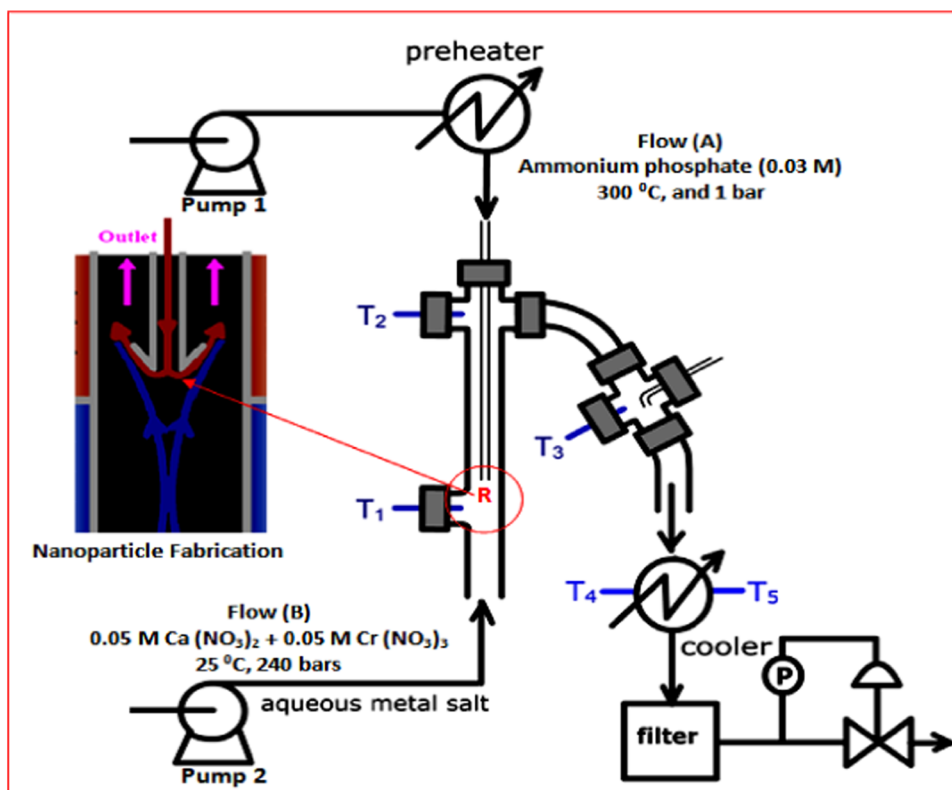
Similar procedures were followed to prepare the Cr-HA/silica sol–gel coating except for the addition of a definite amount of the synthesized nanoparticles (around 2 wt.% of the sample total weight). The added particles were uniformly dispersed into the GPTMS-epoxy mixture through sonication for 30 min before adding the curing agents. Finally, the prepared coatings were applied on the surface of AA2024 coupons at a thickness of $\approx 6 \pm 3$ μm using a spray coater. All coated samples were dried in an oven at 80 °C overnight. Finally, the edges and back surface of the coated samples were waxed using a melting mixture of calphony and beeswax (1:1 wt.%) allowing the exposed area (working electrode) to be 7 ± 1 cm^2.

2.5 Characterization

The morphology of the developed Cr-HA nanoparticles was investigated via TEM (2100, Joel, Japan) and SEM (Zeiss EVO-10, Germany). The latter was equipped with the energy-dispersive X-ray (EDX) detector to investigate the composition of the samples. To examine the crystal morphology at higher resolution and magnification, the SEM was operated on both secondary electron and backscattered modes. Bruker D8 Advance X-ray diffractometer equipped with LYNXEYE linear position-sensitive detector (Bruker AXS, Madison, WI) was used to record the X-ray diffraction (XRD) patterns. Data was collected over a *2θ*-range of 5°–70° at an increment of

0.02° and a scanning rate of 0.2° s^{-1}. In the diffractometer, a Cu-K$_\alpha$ source ($\lambda = 1.5406$ Å) was operated at a tube voltage and current of 40 kV and 40 mA, respectively. A thin layer of a powder sample was placed on a silicon crystal plate supported on a cup to record the patterns.

Fourier-transform Infrared (FTIR) spectra were conducted using a full range scan (4000–400 cm^{-1}) by Jasco-4100 instrument. The background was taken into consideration and both sample and background were measured with a resolution of less than 4 cm^{-1}. Averaged data were calculated using 64 scans.

The crystal structure of the synthesized Cr-substituted HA nanocomposite was determined using the Reflex module available in the Materials Studio package (Version 20.1.0.2728, BIOVIA, USA) [49], along with QualX software (Version 2.24) [50]. The procedure included two stages: first, the experimental powder diffraction pattern was exported to QualX software to search the database for reference patterns (trial structure). Based on the average differences in peak position and the average differences in peak intensity, the candidate structure, which was pure hydroxyapatite with five different Ca sites, was downloaded from Cambridge Crystallography Open Database (COD) [51, 52]. The candidate structure was exported to Materials Studio. In the second stage, five trial structures were built by substituting one of the Ca^{2+} ions, located at different lattice sites [Ca(1), Ca(2), Ca(3), Ca(4), and Ca(5)], with Cr^{3+} ion. Rietveld refinement was

performed on each trial structure to find out the most probable structure, that has a simulated pattern best matches the experimental one [53]. In Rietveld refinement, the profile parameters, cell parameters, and atomic coordinates were all simultaneously refined. A pseudo-Voigt function for profile shape and Finger–Cox–Jephcoat correction for asymmetry at the low-angle region (up to 30°) were used.

2.6 Corrosion evaluation

Potentiostat/galvanostat (reference 600 Gamry™) was used to perform the electrochemical corrosion experiments. EIS experiments were conducted for metal working electrode at room temperature using a fresh 3.5% NaCl aerated solution with a volume/sample surface area ratio not less than $40\,ml/cm^2$. A conventional three-electrode polarization cell was used with coated AA2024 sample working electrode, a platinum counter electrode, and a saturated calomel reference electrode (SCE). The EIS measurements were carried out using an AC signal at OCP from 0.3×10^5 to 10^{-2} Hz frequency range with amplitude of 10 mV peak-to-peak.

To guarantee the reproducibility of the results, every experiment was conducted a minimum of three times at room temperature ($25 \pm 2\,°C$). The electrochemical results obtained from the experiments were graphed through the utilization of Sigma-Plot software.

3 Results and discussion

3.1 Sample characterization

Transmision Electron Microscope (TEM) imaging process was applied to assess the exact shape and average particle size of the synthesized Cr-HA nanoparticles. Cr-HA demonstrated the shape of nanorods (about 20 nm width and 6 μm length as shown in Fig. 2. TEM micrographs demonstrated homogeneity regarding both the shape and the size of the nanorods; this can be correlated to the fixed synthesis conditions.

SEM micrographs of the Cr-HA nanocomposite confirmed the development of high-quality mono-dispersed nanorods (Fig. 3a, b). Elemental mapping via EDX detector showed the uniform distribution of chromium ions within the HA matrix (Fig. 3c). The distribution of the main elements (Cr, Ca, P, and O) within Cr-substituted HA nanoparticles. The elemental mapping manifested the uniform distribution of Cr-HA main elements and the absence of any foreign elements. Although, EDX analysis is a semi-quantitative technique, the quantification of elemental composition was conducted for a matter of comparison to assess the degree of Ca replacement with Cr. EDX analysis indicated that Cr/Ca ratio is ≈1:4 (Fig. 3d).
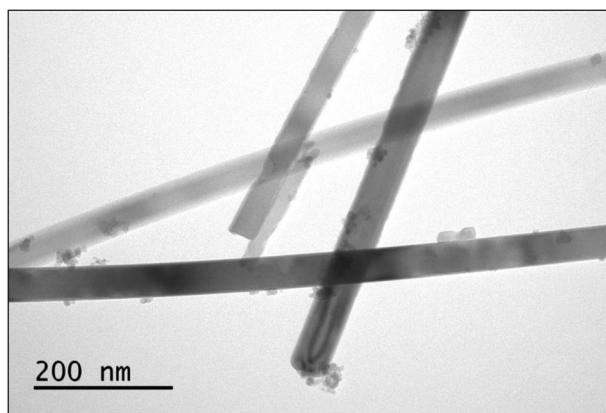

Fig. 2 TEM micrographs of Cr-HA nanocomposite at different magnifications

FTIR was performed for the prepared samples to investigate the interaction between the Cr-HA nanofiller and silica sol–gel coating. Spectra of Cr-HA, neat sol–gel coat, and Cr-HA/sol–gel coat were examined and compared as depicted in Fig. 4. Identification of each sample was conducted by investigating each precursor's spectrum and comparing it with reference structural bands.

Cr-HA nanoparticles displayed characteristic bands at $523\,cm^{-1}$, and $1038\,cm^{-1}$ that were attributed to the asymmetric bending vibration of HPO_4^{2-} and asymmetric stretching of PO_4^{3-} groups respectively [54, 55]. A strong broad band at $3402\,cm^{-1}$ refers to the stretching mode of OH^- in the sample [56, 57].

Silica sol–gel demonstrated bands at 2927 and $2869\,cm^{-1}$ that were related to the symmetric stretching vibration of the C–H bonds in the cured epoxy matrix, while the band at $2927\,cm^{-1}$ was attributed to the asymmetric stretching vibration of the C–H bond [58]. Asymmetric vibration mode at $950\,cm^{-1}$ was related to Si–OH. In addition, the noticed band at $3424\,cm^{-1}$ might be assigned to the OH group of Si–OH found in the uncondensed phase or the hydroxyl group of the physically absorbed water in the sol–gel matrix [59]. The main matrix precursor of the silica sol–gel is essentially based on GLYMO which contains Si–O–C in the epoxide ring that appears at $1200–1000\,cm^{-1}$ band and also this range is referred to Si–O–Si condensed phase [60, 61]. Cr-HA hybrid spectra are highly matched with neat silica spectra, thus no chemical interaction took place, and the dominant component in the Cr-HA hybrid is the silica sol–gel. This is consistent with the percentage added amount of Cr-HA 2% to the sol–gel matrix.

XRD diffractograms demonstrated the evolution of highly crystalline material. The search match results of QualX software revealed that the experimental XRD pattern is similar to that of pure calcium hydroxyapatite (chemical formula $Ca_5(PO_4)_3(OH)$, COD ID 7217892) [62], giving
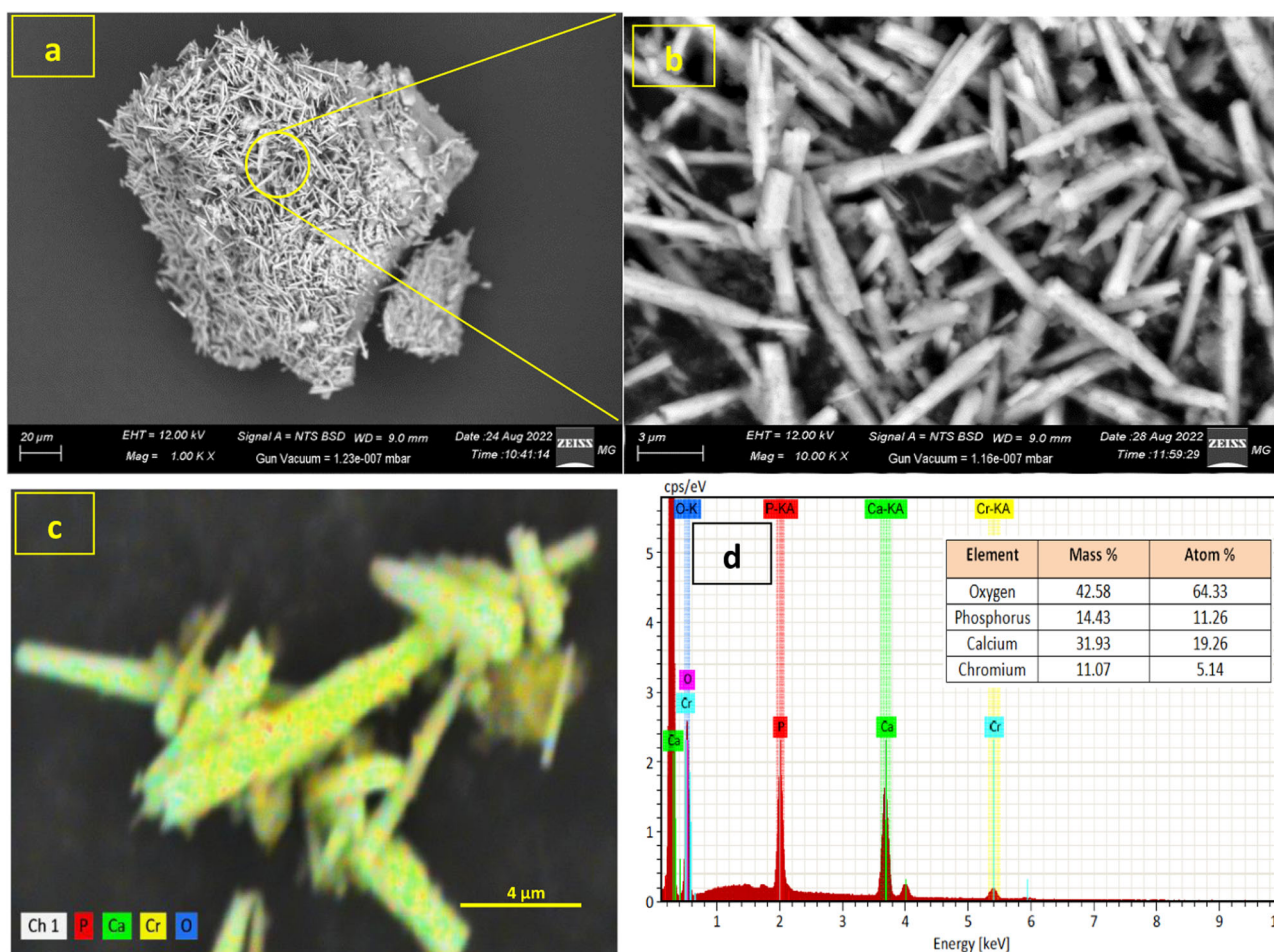
Fig. 3 SEM images of the Cr-HA samples at different magnifications (**a**, **b**), Elemental mapping of Cr-HA nanocomposite (**c**), and quantification of the elemental composition (**d**)
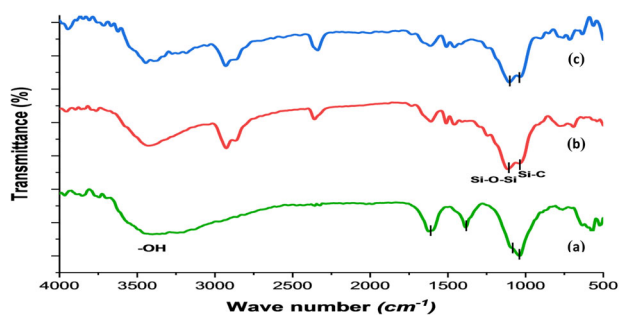

Fig. 4 FTIR spectra of (**a**) Cr/HA, (**b**) neat silica Sol–gel and (**c**) Cr-HA/ sol–gel

FoM = 0.91. All characteristic peaks were matched with those of the selected card indicating the absence of other commonly coexisting phases (α-tricalcium phosphate or β-tricalcium phosphate) (Fig. 5).

According to EDX results, the Ca/Cr atomic ratio shows that Cr substituted one of the five Ca ions in the HA lattice. To electroneutralize the excessive charge encountered by the Cr^{3+} ion, a mechanism was proposed analogous to the substitution reaction of Eu^{3+} and Ca^{2+} in the hydroxyapatite crystal structure, whereby the OH^- transforms into O^{2-} [63]:

$$Cr_2O_3 + 2Ca^{2+} + 2OH^- \rightarrow 2CaO + H_2O + 2Cr^{3+} + 2O^{2-}$$
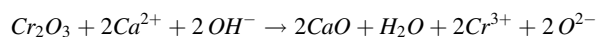
Unlike metal-substituted α- and β- tricalcium phosphate, metal-substituted hydroxyapatite is less soluble and characterized by a long-term release of metal ions [53].

According to the simulation results of Rietveld refinement, the most perspective structure (with $R_{wp} = 9.00\%$) was obtained when Cr ion substituted Ca(1). Figure 6 compares both the experimental diffraction pattern and the simulated pattern of the proposed structure.

The sharp peaks recorded in the XRD diffraction pattern manifest the high degree of crystallinity of the synthesized material. Moreover, the experimental and simulated diffraction patterns were found to be in good agreement implying the success of Rietveld refinement. Table 1 displays the characteristics of the proposed crystal structure.
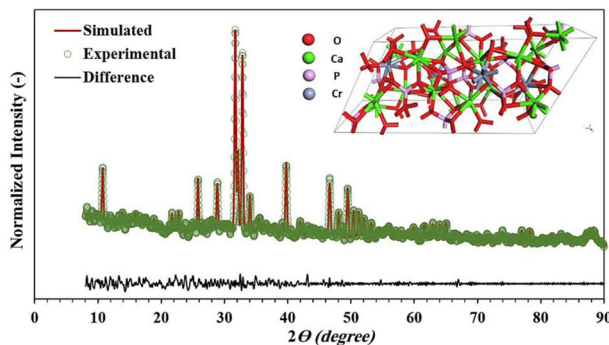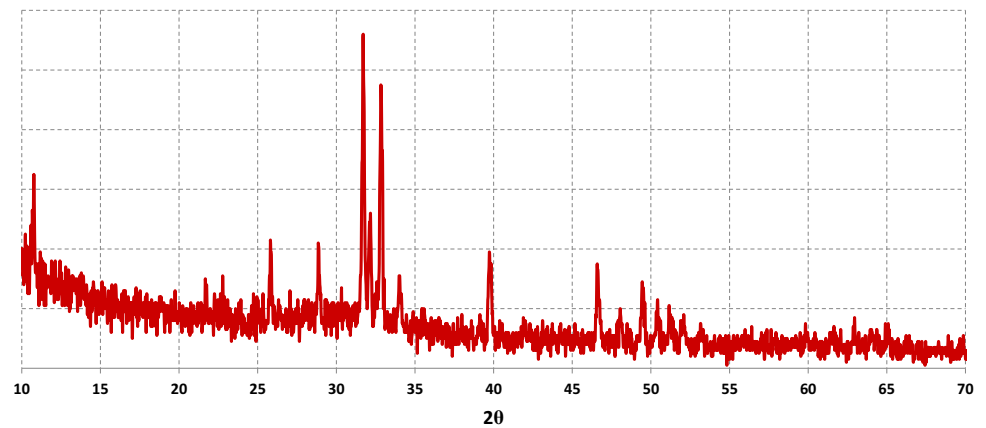
Fig. 5 XRD spectra of Cr-HA nanocomposite

Fig. 6 Comparison between experimental and simulated diffraction spectra

Cr-HA nanoparticles have a monoclinic crystal structure and P 1 1 21/B space group. The cell has a volume of 1055.66 A^3, a theoretical density of ~3.229 g/cm^3, and encloses four asymmetric units (each unit consists of four Ca^{2+} ions, one Cr^{3+} ion, one O^{2-} ion, and three PO_4^{3-} groups). Tables 2 and 3 list the refined profile parameters and the atomic coordinates of the asymmetric unit, respectively.

The coating thickness is very critical since it affects the corrosion behavior of the coated metals particularly when the coating is used as a pre-treatment. The coating thickness was measured using Kett model LZ-330C, where the thicknesses were 6 ± 3 μm for both coating systems. These thicknesses were confirmed using SEM/EDX microscopy.

The cross-section SEM images of the Cr-HA sol–gel sample are demonstrated in Fig. 7. It is obvious that the coating thickness is ≈6 μm as shown in Fig. 7a. SEM micrographs depict that the coating is free of voids and the line scan across the coating clarifies that there is no distinguishable sharp edge between the metal/coating interface as indicated in Fig. 7b–d. This may be relevant to the development of covalent bonds between the silica sol–gel coating and aluminum alloy surface as indicated in the previous studies [64, 65]. As a result, the coating adhesion increases, and its corrosion resistance improves [64, 65].

That bond would enhance the adhesion and bonding as seen by SEM and indicated by line-scan EDX. The figure also clarifies the distribution of intermetallic particles (IMPs) within the Al matrix. The main aim of Fig. 7 is to clarify the good adhesion between metal and coating which clarified by losing the sharp boundary between coating and metal.

3.2 Corrosion performance

In an aerated chloride-containing environment, AA2xxx (aluminum/copper) alloys are susceptible to pitting corrosion due to the heterogeneous composition of the surface [66–69]. The surface heterogeneity arises from the existence of intermetallic particles (IMPs), containing Cu, Mn, Fe, and Mg. Since the corrosion potentials of IMPs are usually higher than that of the base metal, micro galvanic cells are formed [70]. The anodic site of the produced galvanic cell is the aluminum matrix while the IMPs will represent the cathode one. Oxygen reduction reaction would occur on the surface of the IMPs (cathode), whereas the adjacent area to these sites would experience severe corrosion [71, 72]. However, it is worth mentioning that the presence of such intermetallic particles within the aluminum matrix, which represent up to 3% of the alloy, improves the alloy's mechanical properties.

The corrosion protection of the coated samples was assessed via electrochemical impedance spectroscopy (EIS). It is a non-destructive technique commonly used to study the corrosion kinetics of samples over the test course. The test was performed for both neat and Cr-HA/sol–gel coatings during their immersion in artificial seawater and was conducted based on Bode plots for selective immersion time.

Silica sol–gel coating has been applied for corrosion protection of AA2024 comprising active material acting as inhibitor [26, 73, 74]. Compared to traditional inorganic-based sol–gel coatings, hybrid sol–gel coatings are distinguished by their higher corrosion resistance and mechanical properties. Normally, these coatings are applied

Table 1 Characteristics of the crystal structure of Cr-substituted hydroxyapatite

Empirical formula	Ca$_4$Cr(PO$_4$)$_3$(O)	Z	4
Crystal system	Monoclinic	Cell Volume [A$^{\circ 3}$]	1055.66
Space group	P 1 1 21/B	Density [g/cm^3]	3.22917
a [A$^\circ$]	9.40500 ± 0.00132	2θ Range [degrees]	8.00 – 90.00
b [A$^\circ$]	18.83425 ± 0.00375	Step Size [degrees]	0.02
c [A$^\circ$]	6.87308 ± 0.00069	Step Scan Time [s]	10
α [A$^\circ$]	90.00000	No. of Reflections	861
β [A$^\circ$]	90.00000	Final R_p	6.19%
γ [A$^\circ$]	119.87705 ± 0.01600	Final R_{wp}	9.00%

Table 2 Refined profile parameters of Cr-HA nanocomposite

FWHM	
U	0.32481 ± 0.04767
V	−0.11429 ± 0.03413
W	0.07022 ± 0.00642
Profile: Function: Pseudo-Voigt	
NA	0.04277 ± 0.006640
NB	0.00000 ± 0.00171
Line Shift: Instrument Geometry: Bragg–Brentano	
Zero Point	−0.08133 ± 0.00358
Asymmetry Correction: Finger–Cox–Jephcoat 2θ Limit: 30 (degrees)	
H/L	0.01175 ± 0.00209
S/L	0.01119 ± 0.00204

Table 3 The atomic coordinates of the asymmetric unit of Cr-HA nanocomposite

Atom name	Coordinates [A$^\circ$]			Occupancy
	X	Y	Z	
Cr(1)	0.36139	0.59452	0.02326	1
Ca(2)	0.33633	0.58375	0.52753	1
Ca(3)	0.23352	0.24756	0.22880	1
Ca(4)	−0.01552	0.62030	0.74278	1
Ca(5)	0.27258	0.37731	0.75421	1
P(1)	0.38482	0.43913	0.22256	1
P(2)	0.61996	0.26482	0.27108	1
P(3)	0.04683	0.45001	0.75701	1

at low temperatures to create a cross-linked film [26]. Usually neat silica sol–gel coating (without inhibitor) acts as a barrier coating, but fails to protect metals from corrosion for long periods [75].

Regarding the neat silica sol–gel coated sample (Fig. 8), the impedance showed a linear trend during the first few hours of immersion with a slope approaching −1 over the high-frequency range as shown in Fig. 8a. Such a trend indicates a general capacitive behavior and implies a hydrophobic nature of silica sol–gel coating [75–77]. The coating exhibited a single-time constant at this stage. Later on, the capacitive behavior changed to be resistive and the total impedance at 10^{-2} Hz experienced a dramatic decrease (one order of magnitude) after 24 h of immersion. Moreover, a new time constant appeared at the mid-frequency range and continued to increase and shifted to the higher frequency range. This response reflects the gradual diffusion of the corrosive solution through the coating layer.

Two-time constants (at high- and mid-frequency ranges) were clearly noticed during the early stage of immersion as shown in Fig. 8b. The former corresponds to the dielectric property of the porous silica sol–gel layer, while the latter represents the barrier layer. The peak position of the mid-range time constant shifted to higher frequencies indicating the penetration of the coating by the electrolyte [78, 79]. This behavior is due to the porous properties of neat silica sol–gel coating [80, 81] which represents a typical behavior of inactive barrier coating. For any inactive barrier coating, after a while of immersion in an aqueous electrolyte, the electrolyte ingresses through the coating layer into the metal/coating interface and finally affects the metal surface.

In this case of neat sol–gel coating, the electrolyte diffused through the coating layer and water uptake increased as indicated by the continuous decrease of impedance and increase of the time constant in the mid-frequency range. After five days of immersion, the electrolyte reached the metal surface and the corrosion process started to occur resulting in the appearance of a new time constant at the low-frequency range (metal/coating interface).

In our previous work [75], similar behaviors and results were obtained when silica sol–gel coating was applied on the same alloy and immersed in a 3.5% NaCl solution. The only difference was the coating thickness (15 ± 2 μm), which extended the time of diffusion of the corrosive electrolyte through it. Consequently, the pitting corrosion was observed after a longer period (10 days) of immersion. In another study, the same behavior of continuous decreasing in the impedance during immersion of neat silica sol–gel coated AA2024 was also perceived [82], even

Fig. 7 SEM images of (**a**) Cr-HA/sol–gel cross-section coated AA2024 samples with their (**b**) Al, (**c**) Si elemental EDX mapping, and (**d**) EDX line analysis
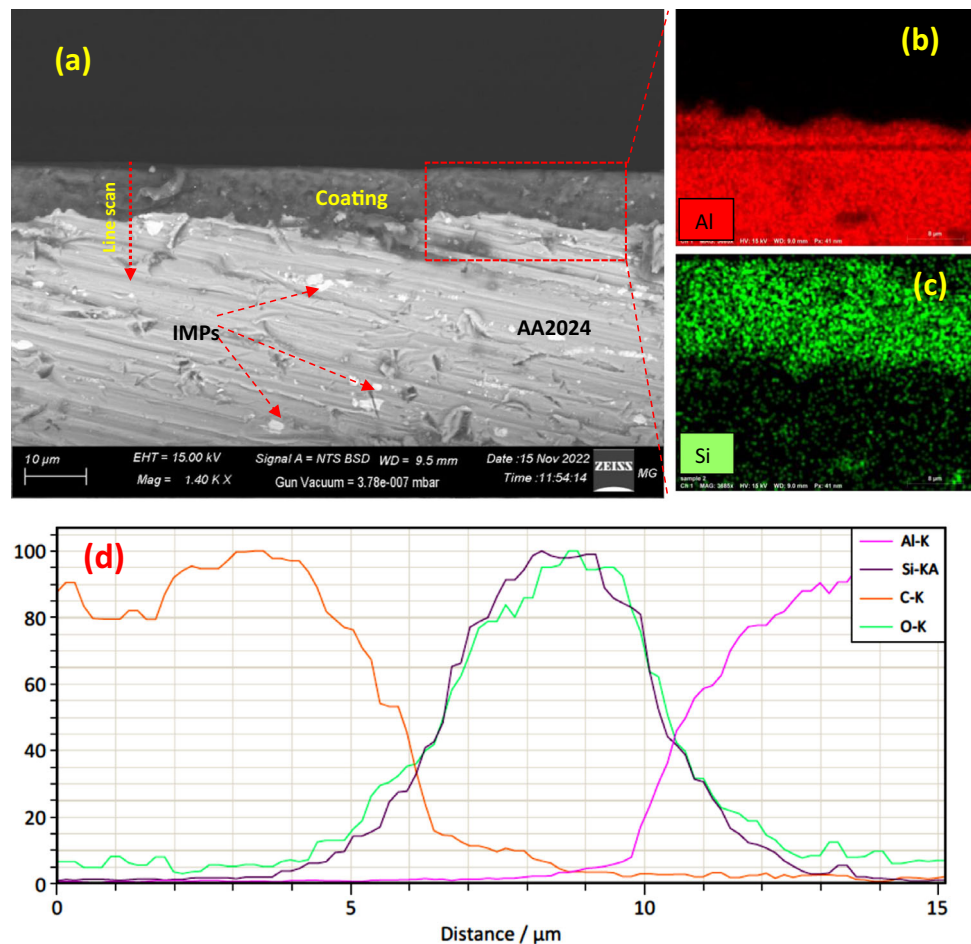
though, the silica coating was applied as post-treatment (sealant) for the plasma electrolytic oxidation.

Also, the corrosion resistance of a neat silica sol–gel coated AA2024 showed a gradual decrease in artificial acidic rain [26]. Despite the same range of the initial impedance values with our current study, the coating withstood a longer time in the immersion test.

This corrosion behavior was characterized by the appearance of dark spots on the coating surface, (Fig. 9a) which turned into brown color after ten days of immersion (Fig. 9b). This observation confirms the EIS results indicating the commencement of pitting corrosion and deterioration of the coating.

The EDX elemental mapping of the surface of the sol–gel coated sample after 15 days of immersion in 3.5% NaCl aerated solution is shown in Fig. 10. The mapping clearly shows that the pitting occurs in the vicinity of the IMPs sites.

Although the corrosion behavior of both Cr-HA /sol–gel and neat sol–gel coated samples was similar during the first 24 h, the former behaved differently during the rest of the immersion course as shown in Fig. 11a. The total impedance showed a sharp drop in the early stage of immersion

(from $2\,M\Omega.cm^2$ to $0.8\,M\Omega.cm^2$) with a single time constant that moved to a higher frequency range as shown in Fig. 11b. In addition, the capacitive behavior of this coating changed to a resistive one during the early stage of immersion. The impedance values at the mid and high-frequency ranges continuously decreased during the first few days of immersion. This behavior occurred due to the increase in electrolyte uptake and is associated with the shift of the time constant from the mid to the high-frequency range. However, after three weeks of immersion, the water uptake reached equilibrium and the coating could not intake more electrolyte as indicated by the stability of the time constant.

On the contrary to neat sol–gel, it showed a continuous capacitive performance over the low-frequency range and this behavior lasted till the end of the test (110 days). Generally, the total impedance, |Z| values at 10 mHz, of the Cr-HA/sol–gel coated sample is not so different from that of the neat. Actually, the amount of Cr-HA is 2% within the sol–gel coating matrix which did not markedly affect the coating thickness; consequently, it would not affect the total impedance of both coating systems. With contentious immersion, the barrier properties of the

Fig. 8 Impedance plots, where (**a**) Phase angel plots, and (**b**) of sol–gel coated AA2024 in 3.5% NaCl
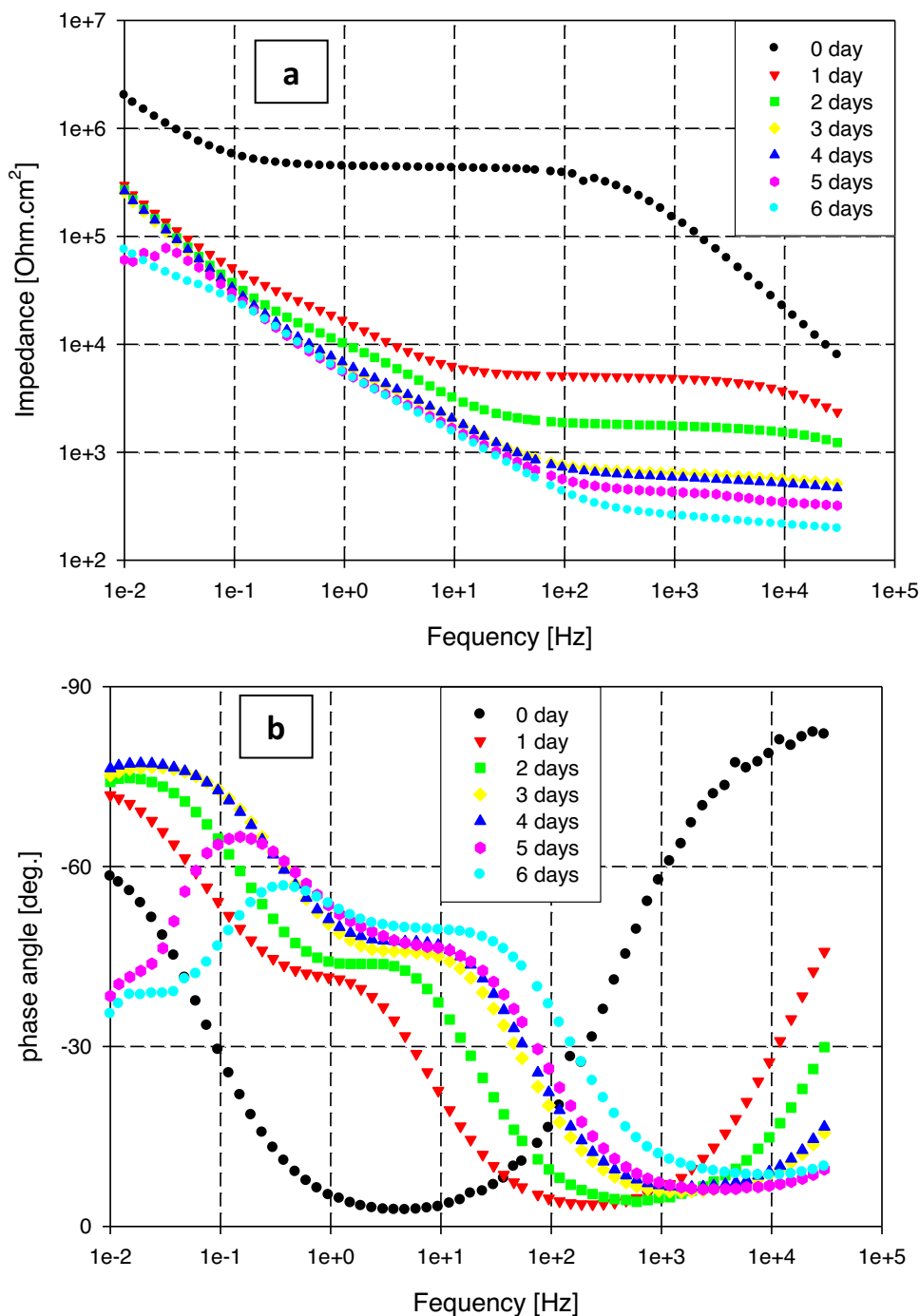
coating decreased and the effect of active material (Cr-HA) was clarified. It seems that there are two overlapped time constants over the low-frequency range. By increasing the immersion time, these two time constants become separated. The two time constants appearing around 0.1 Hz and 3 Hz represent the coating/metal and coating/electrolyte interfaces, respectively. The former time constant steadily moves to a higher frequency and its peak slightly decreases as immersion time increases. This

behavior suggests the formation of an interfacial layer at the coating/metal interface which improves the corrosion resistance of the coated sample [72]. Although the impedance at both mid- and high-frequency ranges was slightly reduced, the total impedance (|Z| at 0.01 Hz) remained almost unchanged throughout the entire immersion time.

The optical examination of the Cr-HA/sol–gel coated sample showed no signs of corrosion or delamination

Fig. 9 Optical image of sol–gel coated AA2024 after (**a**) 6 days (**b**) 12 days in 3.5% NaCl
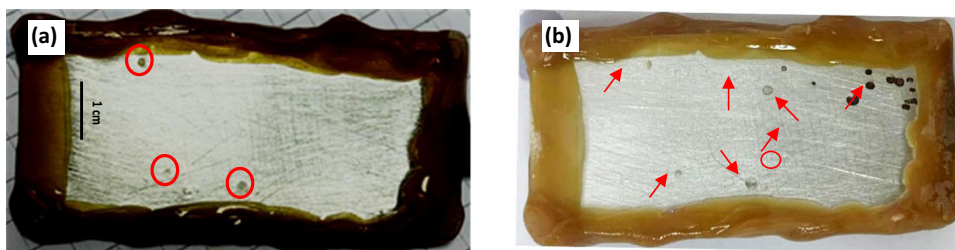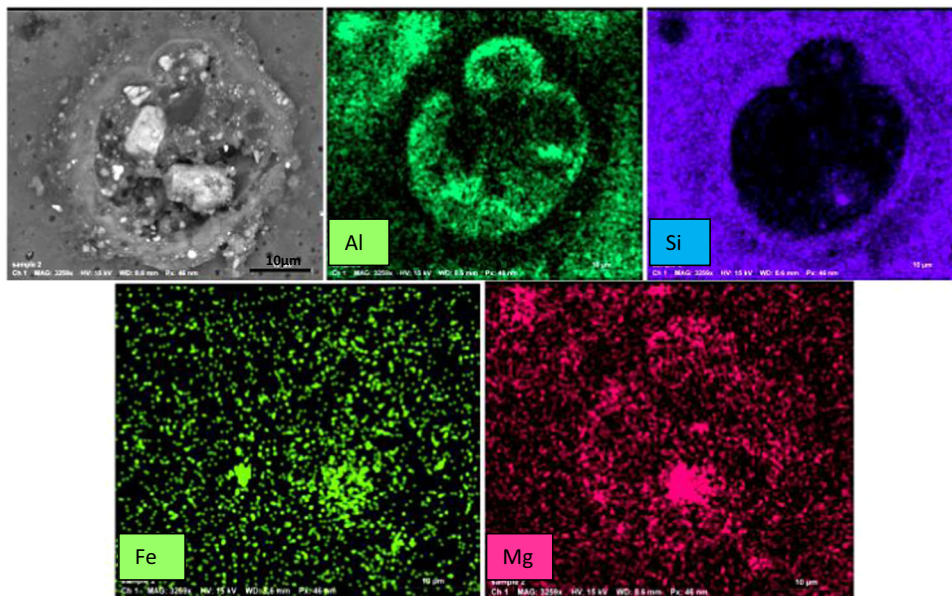

Fig. 10 EDX elemental mapping sol–gel coated AA2024 samples after 15 days of immersion in 3.5% NaCl solution
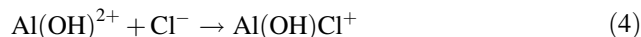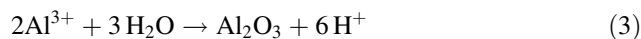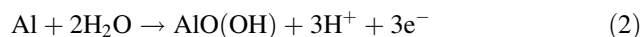
during the test period (Fig. 12). Also, Supplementary Fig. S1 showed the SEM image of the coated surface after immersed in the corrosive solution for 5 days where no sign of corrosion were appeared.

With reference to our previous study [31], it turns out that incorporating Cr-HA nanoparticles into a silica sol–gel matrix can offer extended corrosion protection to neat silica sol–gel coating. It is known that HA improves the corrosion resistance of AA2024 in artificial seawater. The nanoplates geometry of HA crystals seems to play a key role in increasing the barrier property of silica sol–gel coating. Moreover, the incorporation of Cr into the HA crystal structure has an additional impact on the corrosion resistance of AA2024 in the same corrosive electrolyte. The active mechanism of the Cr-HA/silica sol–gel coating will be discussed in the following part.

For a better understanding of the corrosion protection mechanism of Cr-HA/sol–gel coating, the corrosion mechanism of AA2024 should be discussed in advance. As mentioned before, the presence of intermetallic particles (IMPs) in AA2024 aluminum alloy, similar to that presented in Fig. 7a, leads to improved mechanical properties. Unfortunately, these particles negatively affect the corrosion behavior of the alloy by altering the

homogenous potential of the alloy's surface [66, 67]. This alloy is usually prone to pitting corrosion in aqueous chloride solution and the pitting degree is governed by the intermetallic particles' nature [70]. Generally, under open circuit conditions, the S-phase, Al_2CuMg, particles have less potential than that of the base metal due to the presence of highly active magnesium metal. Accordingly, Mg selectively dissolves leaving high potential particles (typically copper) representing the cathode sites where the reduction reaction of oxygen occurs. The oxidation reaction (Al matrix dissolution) takes place as consecutive reactions forming a soluble complex $(Al(OH)Cl^+)$ [83].

$$Al + 3H_2O \rightarrow Al(OH)_3 + 3H^+ + 3e^- \quad (1)$$

$$Al + 2H_2O \rightarrow AlO(OH) + 3H^+ + 3e^- \quad (2)$$

$$2Al^{3+} + 3H_2O \rightarrow Al_2O_3 + 6H^+ \quad (3)$$

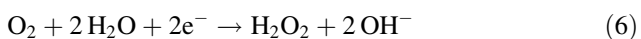$$Al(OH)^{2+} + Cl^- \rightarrow Al(OH)Cl^+ \quad (4)$$

Meanwhile, oxygen undergoes reduction at the cathodic sites (IMP) producing OH^- which would increase the local

Fig. 11 Impedance module plots (**a**) phase plots (**b**) of Cr-HA/ sol–gel coated AA2024 samples in 3.5% NaCl solution at room temperature
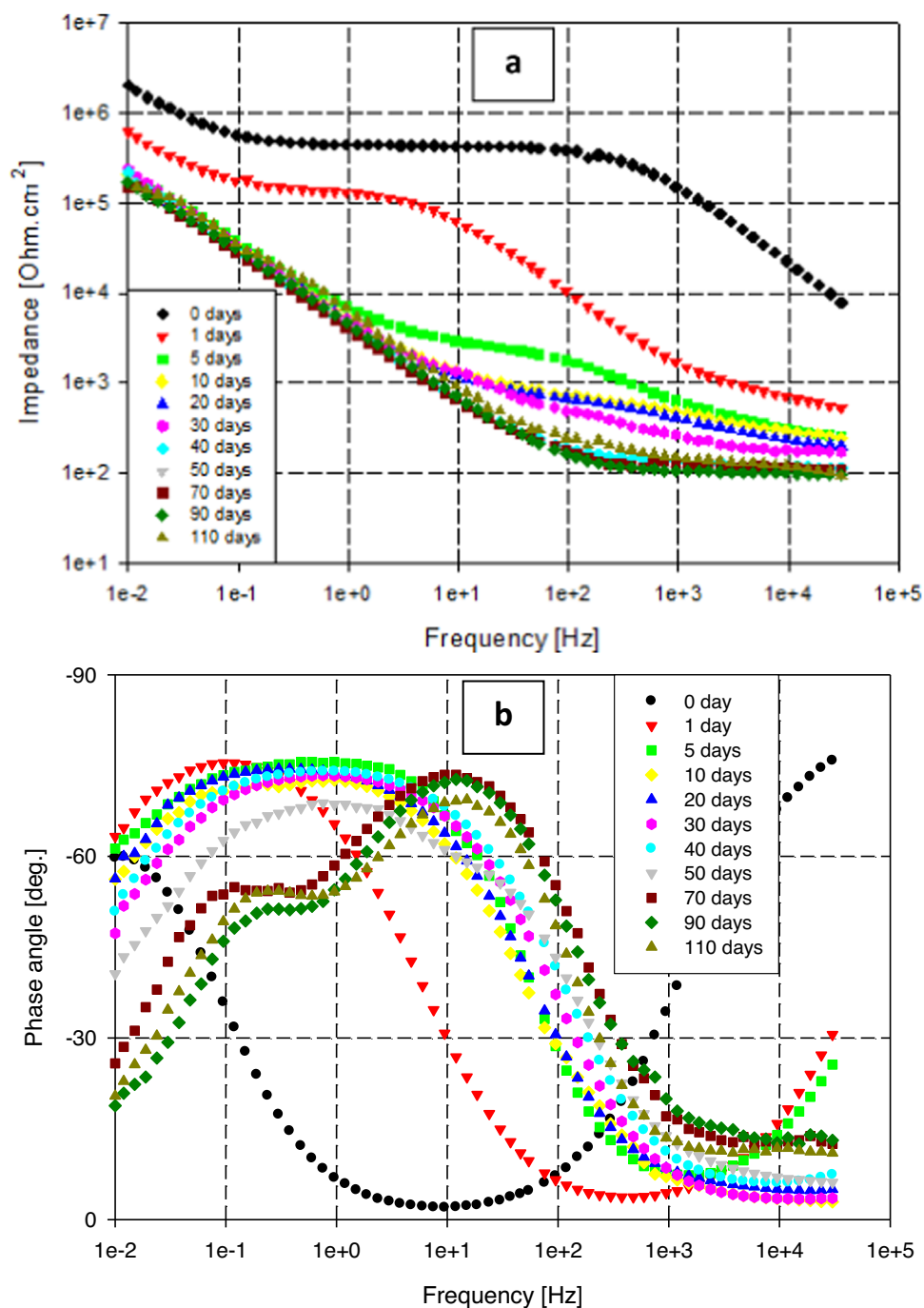
pH and also form some intermediates such as H_2O_2:

$$\tfrac{1}{2} O_2 + H_2O + 2e^- \rightarrow 2OH^- \tag{5}$$

$$O_2 + 2 H_2O + 2e^- \rightarrow H_2O_2 + 2 OH^- \tag{6}$$

The reduction potential of H_2O_2 is greater than that of O_2 (1.76 V and 1.23 V vs SHE respectively). Consequently, any oxidation reaction would take place nearby the H_2O_2 production sites, i.e. IMPs. The produced H_2O_2, localized around the Cu-rich IMP, would partially oxidize Cr(III) atoms within HA-Cr nanoparticles forming Cr(VI) [84, 85]. Generally, chromium [Cr(III,VI)] is present as mixed chromates and/or oxides, accounting for the stability of the coating. Li et al. [86] proposed that chromates diffused onto the corroded sites forming a passivating layer. In addition, the buffering action of HA particles stabilizes the pH over the AA2024 surface and controls the local dissolution of the aluminum matrix [87, 88]. As a result, the autocatalytic mechanism of pitting corrosion can be greatly impeded.

The EIS data were interpreted by two methods; evaluating the low-frequency impedance values obtained from the spectra, and modeling the protective coating using an equivalent circuit. The process of fitting the EIS data with equivalent electrical circuits supports the comprehension of the corrosion mechanism. According to Akid et al. [89, 90], silica sol–gel coating forms two layers when applied on an AA2024 substrate; an outer layer and an inner nano-interfacial layer bonded to the surface. In this context, the equivalent circuits shown in Fig. 13a, b are used for simulation and fitting the obtained EIS data of the coated AA2024 before and after immersion. The proposed equivalent circuit consists of the following: (i) a solution resistance (R_s); (ii) a sol–gel layer consisting of a coating capacitor (C_o) in parallel with a resistance (R_o) representing the pores or defects in the sol–gel coating layer and (iii) an inner layer represented by a capacitor (C_c) in parallel with a resistance (R_c). After 5 days of immersion, the electrolyte continues to diffuse through the silica sol–gel coating layer and finally reaches the metal/coating interface yielding an impedance decrease over the entire frequency range. Following immersion, and in the presence of active species, such as Cr, the corrosive solution reaches the metal surface forming a protective passive layer which can be represented by a capacitor (C_p) and a resistance (R_p) connected in parallel. In the above plots, the phase angle does not reach 90°, therefore, constant phase elements (CPE) were used instead of pure capacitances to obtain good agreement between the
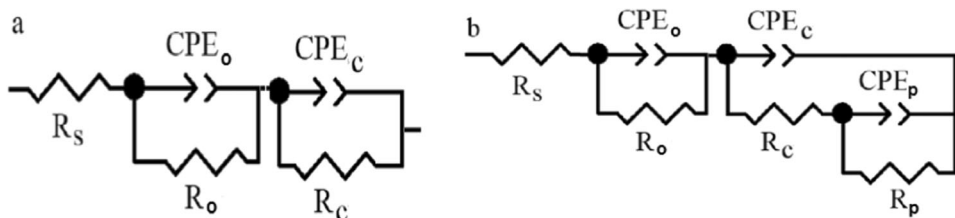
simulated and experimental data. The impedance of CPE was calculated according to the following equation;

$$Z_{CPE} = \frac{1}{(j\omega)^n Q}$$

where Q is the parameter related to the electrode capacitance (F.s^{n-1}/cm^2), n is the constant phase exponent ($0 < n < 1$) related to the deviation of the straight capacitive line from 90°, j is the imaginary number ($j = \sqrt{-1}$) and ω is the angular frequency ($\omega = 2\pi f$, f is the frequency) [91].

The fitting parameters of the EIS tests for the Cr-HA/sol–gel coated AA2024 following immersion in 3.5% NaCl solutions are represented in Supplementary Table S1. The table also contains the discrepancy between the model and the expiremental data (Chi- square) from the Nyquist plots. Moreover, a comparison of selected experimental and modeled data of the EIS tests is given in Supplementary Fig. S2.

The results of experimental data fitting are displayed in Fig. 14a–c. After a few hours and up to five days of immersion, the coating layer resistance sharply decreased (both the inner and outer layer resistance lost about one order of magnitude) whereby the corrosive solution started to break through the coating layer without reaching the metal surface thanks to the sol–gel barrier properties. After five days, the electrolyte continued to diffuse through the coating and reached the metal surface where a reaction between the coating, metal, and electrolyte took place. Correspondingly, a new protective layer is formed at the coating/metal interface resulting in the recovery of part of the resistance of the sol–gel layer. The metal continued to be protected by both the coating barrier properties and the formed protective layer which maintains stable impedance values over this long course of immersion.

The performance of the protective coating can be also evaluated via studying the breakpoint frequency (f_b) which is correlated to the delaminated areas of organic coatings [92, 93]. The breakpoint frequency has a direct relation to the electrochemically active surface area [94] and consequently, f_b is a useful parameter to assess the degradation of the organic coatings. Its increase with immersion time usually refers to the seepage of the electrolyte to the metal surface. The breakpoint frequency can be taken as the frequency at a 45° phase angle [93, 95, 96].
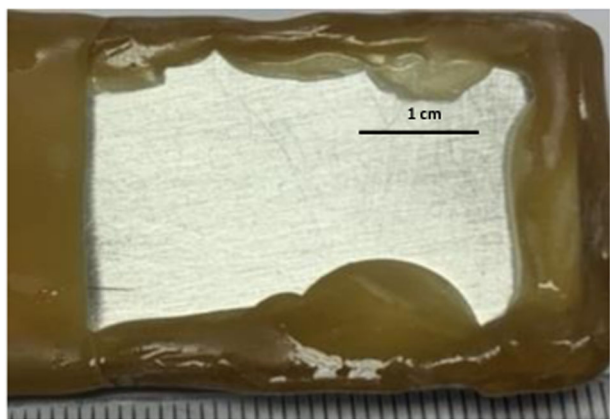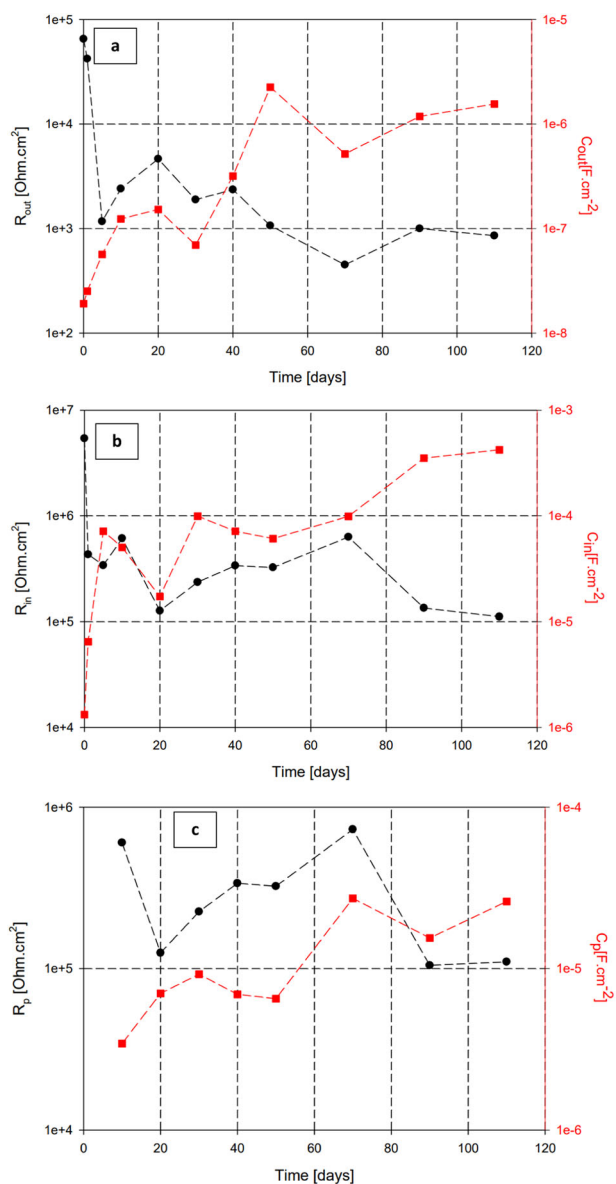

Fig. 12 Optical image of Cr-HA/sol–gel coated AA2024 samples after immersion in 3.5% NaCl solution for 110 days at room temperature

Fig. 13 Fitting equivalent circuits of the EIS data before 5 days (**a**) and after 5 days (**b**) of immersion in 3.5% NaCl solution

Fig. 14 Outer layer Cr-HA/sol–gel coating resistance and capacitance (**a**) interfacial layer resistance and capacitance (**b**) and passive layer resistance and capacitance (**c**) following immersion in 3.5% NaCl solutions

Fig. 15 Changing of breakpoint frequency, f_b, of coating systems with immersion in 3.5% NaCl solution

Although the electrolyte reached the bottom layer of Cr-HA sol–gel coating, it interacted at the interface forming a stable passive layer preventing the corrosion process. Owing to the activity of Cr (III) within Cr-HA incorporated into the coating, a compact passive film is produced at the penetrated coating/metal interface.

The earlier section clearly revealed that the Cr-HA nanoparticles within the sol–gel matrix significantly enhanced the corrosion resistance of AA2024 in artificial seawater. The presence of Cr(III) within the sol–gel coating reduces the cathodic reduction reactions (oxygen reduction reaction). The chromate species precipitated on the cathodic (IMPs) sites as a result of Cr (III)/metal interactions. This precipitation forms a stable film decreasing the galvanic current of the metal surface [97]. The mass transfer rate of Cr species from the coating matrix to the IMPs surface is considered the rate-determining step forming the film [98]. This chromate film can impede the adsorption of oxygen on the IMPs resulting in a noticeable corrosion hindrance in this aqueous 3.5% NaCl solution [99, 100].

3.3 Evaluation of active corrosion protection on artificially damaged substrates

Cr-HA/sol–gel coated sample was scratched to investigate the self-healing capability of the coating using the EIS technique for assessment. The coated sample was immersed in a 3.5% NaCl corrosive solution for three days and the EIS measurement was conducted. After that, the sample was scratched using a razor, immersed in the corrosive electrolyte, and retested over a selected period. The impedance curve, Fig. 16a, shows that the impedance value of the coated AA2024 sample sharply decreased after scratching and lost about one and a half orders of magnitude after one min because of the direct exposure of the metal surface to the electrolyte. As the immersion time increased, the

The change of f_b with exposure time for both neat and Cr-HA sol–gel coatings is shown in Fig. 15. The figure shows that f_b of both sol–gel coatings shifted to higher frequencies during the early stage of immersion. This behavior is attributed to the increase of coating penetration by aqueous electrolyte resulting in the reduction of impedance and finally coating degradation. As time elapsed, the interaction of the electrolyte with the metal substrate underneath the neat sol–gel coating causes corrosion. However, due to the presence of Cr-HA in the sol–gel coating, no corrosion products appeared and f_b values remain almost constant over 110 days of immersion.
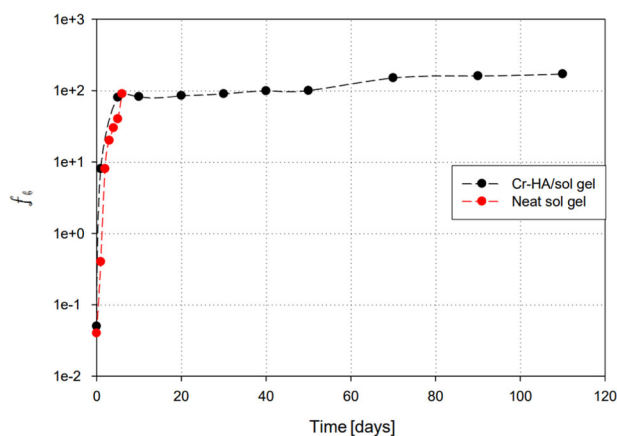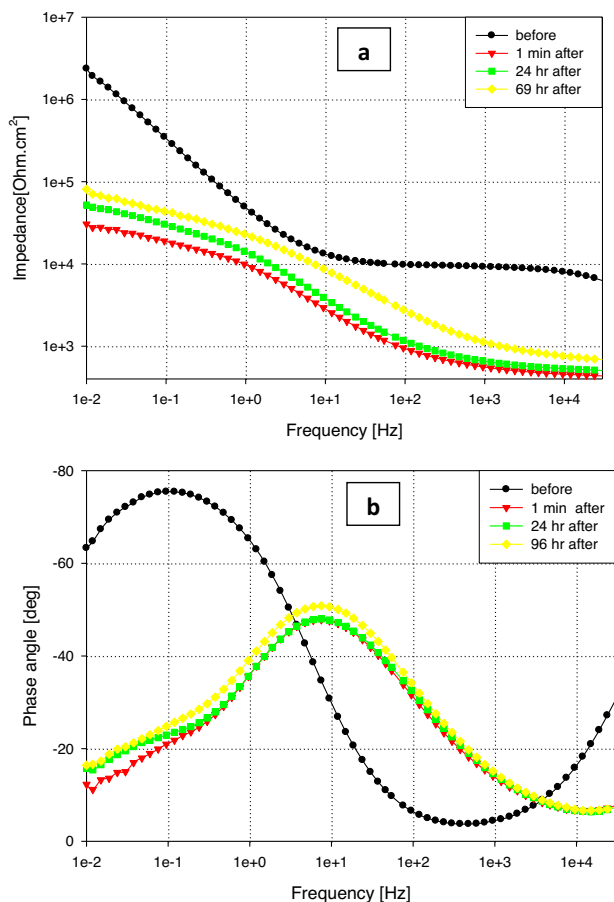
Fig. 16 Impedance plots (**a**) phase plots (**b**) of scratched Cr-HA/sol–gel coated AA2024 samples in 3.5% Na Cl solution at room temperature

impedance began to be retrieved as shown in Fig. 16a. Also, the phase angle of the scratched coated sample, Fig. 16b, showed a single time constant at the mid-frequency range which became more capacitive over time. In addition, the sample did not show any time constant at the low-frequency range (which represents the corrosion process) after scratching the coated metal. These findings indicate that Cr-HA/sol–gel coating might offer a prospective self-healing aspect for AA2024 coated substrate.

4 Conclusions

The continuous hydrothermal synthesis technique offers a facile route to replace the calcium atom in the hydroxyapatite molecular structure with another different atom. In this study, Cr(III) replaces one-quarter of the Ca atoms in the HA molecules. The prepared Cr-HA material has a needle-shaped crystal that uniformly comprises Ca, P, Cr, and O atoms indicating the creation of the novel Cr-HA molecule. In addition, computational software study and

analysis confirm the replacement of the Ca atom by the Cr atom in the hydroxyapatite molecules. Neat silica sol–gel coating is an inert barrier that cannot protect AA2024 in chloride-containing electrolytes. However, composing the sol–gel coating with Cr-HA molecules provides a matrix that is appropriate for extended corrosion protection of AA2024 in artificial seawater. Electrochemical investigation and optical observation suggested the formation of an interfacial protective layer that is responsible for the extended corrosion resistance. The proposed mechanism of protection is suggested to occur via Cr(III)/Cr(IV) redox on the substrate surface. Also, HA molecules have a buffering action stabilizing the surface of the substrate. Finally, the scratch test showed that the Cr-HA material may propose corrosion protection property for AA2024.

Data availability

The datasets generated and/or analyzed during the current study are available in the Cambridge Crystallographic Data Center (CCDC), Deposition Number CCDC **2238411**, https://www.ccdc.cam.ac.uk/structures/Search?Author=ibrahim%20naeem&DatabaseToSearch=Published.

Compliance with ethical standards

Conflict of interest The authors declare no competing interests.

Publisher's note Springer Nature remains neutral with regard to jurisdictional claims in published maps and institutional affiliations.

Supplementary information The online version contains supplementary material available at https://doi.org/10.1007/s10971-023-06187-7.

References

1. Ely M et al. (2017) Role of post-treatment in improved corrosion behavior of trivalent chromium protection (TCP) coating deposited on aluminum alloy 2024-T3. J Electrochem Soc 164(6):C276

2. Hegde M et al. (2022) Abrasion and cavitation erosion resistance of multi-layer dip coated sol-gel coatings on AA2024-T3. Corros Mater Degrad 3(4):661–671

3. Merisalu M et al. (2021) Effective corrosion protection of aluminum alloy AA2024-T3 with novel thin nanostructured oxide coating. Surf Coat Technol 411:126993

4. Nardeli JV et al. (2020) Novel healing coatings based on natural-derived polyurethane modified with tannins for corrosion protection of AA2024-T3. Corros Sci 162:108213

5. Yang Z et al. (2023) A multifunctional Sr (HQ) 2 filler-reinforced coating for self-healing and physical barrier properties on aluminum alloy. Prog Org Coat 180:107567

6. Nardeli JV et al. (2019) Tannin: a natural corrosion inhibitor for aluminum alloys. Prog Org Coat 135:368–381

7. Nardeli JV et al. (2021) Biobased self-healing polyurethane coating with Zn micro-flakes for corrosion protection of AA7475. Chem Eng J 404:126478

8. Mohammadi I et al. (2022) Construction of an epoxy coating with excellent protection performance on the AA 2024-T3 using ion-exchange materials loaded with eco-friendly corrosion inhibitors. Prog Org Coat 166:106786

9. Klumpp RE et al. (2022) A cerium-based nanocoating for corrosion protection of the AA1230 as clad material for the AA2024-T3 alloy. Mater Res. 25:9.

10. Kamaraj K et al. (2012) Electropolymerised polyaniline films as effective replacement of carcinogenic chromate treatments for corrosion protection of aluminium alloys. Synth Met 162(5-6):536–542

11. Subasri R et al. (2019) Environmentally friendly Zn–Al layered double hydroxide (LDH)-based sol–gel corrosion protection coatings on AA 2024-T3. J Coat Technol Res 16(5):1447–1463

12. Visser P, Terryn H, Mol JM (2018) On the importance of irreversibility of corrosion inhibitors for active coating protection of AA2024-T3. Corros Sci 140:272–285

13. Lakshmi RV, Sampath S, Aruna ST (2021) Silica-alumina based sol-gel coating containing cerium oxide nanofibers as a potent alternative to conversion coating for AA2024 alloy. Surf Coat Technol 411:127007

14. Thai TT, Trinh AT, Olivier M-G (2020) Hybrid sol–gel coatings doped with cerium nanocontainers for active corrosion protection of AA2024. Prog Org Coat 138:105428

15. Xue B et al. (2017) Corrosion protection of AA2024-T3 by sol-gel film modified with graphene oxide. J Alloy Compd 725:84–95

16. Voevodin NN, Kurdziel JW, Mantz R (2006) Corrosion protection for aerospace aluminum alloys by Modified Self-assembled NAnophase Particle (MSNAP) sol–gel. Surf Coat Technol 201(3):1080–1084

17. Chaoshuai L et al. (2021) High nanopore volume tetrethoxysilane based aerogels prepared with addition of N, N-dimethylformamide at different stage of the sol-gel process. Mater Sci 27(3):330–333

18. Pirzada T et al. (2020) Cellulose silica hybrid nanofiber aerogels: from sol–gel electrospun nanofibers to multifunctional aerogels. Adv Funct Mater 30(5):1907359

19. Styskalik A et al. (2020) Highly porous hybrid metallosilicate materials prepared by non-hydrolytic sol-gel: Hydrothermal stability and catalytic properties in ethanol dehydration. Microporous Mesoporous Mater 297:110028

20. Poberžnik M et al. (2018) Insight into the bonding of silanols to oxidized aluminum surfaces. J Phys Chem C 122(17):9417–9431

21. Poberžnik M, Kokalj A (2019) Implausibility of bidentate bonding of the silanol headgroup to oxidized aluminum surfaces. Appl Surf Sci 492:909–918

22. Rodič P et al. (2018) Corrosion behaviour and chemical stability of transparent hybrid sol-gel coatings deposited on aluminium in acidic and alkaline solutions. Prog Org Coat 124:286–295

23. Harb SV et al. (2016) A comparative study on graphene oxide and carbon nanotube reinforcement of PMMA-siloxane-silica anticorrosive coatings. ACS Appl Mater Interfaces 8(25):16339–16350

24. Harb SV et al. (2015) Siloxane–PMMA hybrid anti-corrosion coatings reinforced by lignin. Surf Coat Technol 275:9–16

25. Afsharimani N et al. (2020) Hybrid sol–gel silica coatings containing graphene nanosheets for improving the corrosion protection of aa2024-t3. Nanomaterials 10(6):1050

26. Jafari-Tarzanagh Y et al. (2022) Active corrosion protection of AA2024 aluminum alloy by sol-gel coating containing inhibitor-loaded mesoporous SBA-15. Prog Org Coat 173:107166

27. Gautam A et al. (2022) Capped inhibitor-loaded halloysite nanoclay-based self-healing silica coatings for corrosion protection of mild steel. Ceram Int 48(20):30151–30163

28. Suárez-Vega A et al. (2021) Properties of hybrid sol-gel coatings with the incorporation of lanthanum 4-hydroxy cinnamate as corrosion inhibitor on carbon steel with different surface finishes. Appl Surf Sci 561:149881

29. Mohammadpour Z, Zare HR (2021) The role of embedded 2-ABT@Cu-BTC MOF on the anti-corrosion performance of electro-assisted deposited silica sol-gel composite film. Mater Chem Phys 267:124590

30. Lakshmi RV, Aruna ST, Sampath S (2017) Ceria nanoparticles vis-à-vis cerium nitrate as corrosion inhibitors for silica-alumina hybrid sol-gel coating. Appl Surf Sci 393:397–404

31. Gobara M et al. (2018) Novel smart hydroxyapatite/silica sol–gel nanocomposite hybrid coating for corrosion protection of AA2024. J Inorg Organomet Polym Mater 28(4):1598–1608

32. Nenen A et al. (2022) Synthesis of antibacterial silver and zinc doped nano-hydroxyapatite with potential in bone tissue engineering applications. Ceram Int 48(23, Part A):34750–34759

33. Hartati YW et al. (2022) Recent advances in hydroxyapatite-based electrochemical biosensors: applications and future perspectives. Sens Bio Sens Res 38:100542

34. Firdaus Hussin MS et al. (2022) Extraction of natural hydroxyapatite for biomedical applications—a review. Heliyon 8(8):e10356

35. El-Morsy MA et al. (2022) Mixed systems of hydroxyapatite Gallium oxide (Ga2O3)/Graphene oxide for medical applications: antibacterial, mechanical and morphology. Surf Interfaces 35:102461

36. Li Q et al. (2022) Continuous hydrothermal flow synthesis and characterization of ZrO2 nanoparticles doped with CeO2 in supercritical water. Nanomaterials 12(4):668

37. Sierra-Pallares J et al. (2016) Understanding bottom-up continuous hydrothermal synthesis of nanoparticles using empirical measurement and computational simulation. Nano Res 9:3377–3387

38. Darr JA et al. (2017) Continuous hydrothermal synthesis of inorganic nanoparticles: applications and future directions. Chem Rev 117(17):11125–11238

39. Santiago E et al. (2022) Hydrothermal synthesis of fluorapatite coatings over titanium implants for enhanced osseointegration—an in vivo study in the rabbit. J Funct Biomater 13(4):241

40. Jiantao Q et al. (2018) Effect of an Fe (II)-modified trivalent chromium conversion process on Cr (VI) formation during coating of AA 2024 alloy. Electrochem Commun 92:1–4

41. Proença CS et al. (2019) Trivalent chromium conversion coating on AA2024-T3 used in aeronautical and aerospace industry. Surf Interface Anal 51(12):1298–1311

42. Qi J et al. (2021) Formation of a trivalent chromium conversion coating on AZ91D magnesium alloy. Corros Sci 186:109459

43. Nickerson W, Matzdorf C (2012) Non-chromate aluminum pre-treatments. Naval Air Systems Command Patuxent River, MD

44. Mitton DB et al. (2017) Selected Cr (VI) replacement options for aluminum alloys: a literature survey. Corros Rev 35(6):365–381

45. Bouali AC et al. (2020) Layered double hydroxides (LDHs) as functional materials for the corrosion protection of aluminum alloys: A review. Appl Mater Today 21:100857

46. Kwok CT et al. (2009) Characterization and corrosion behavior of hydroxyapatite coatings on Ti6Al4V fabricated by electrophoretic deposition. Appl Surf Sci 255(13-14):6736–6744

47. Hiromoto S, Yamamoto A (2009) High corrosion resistance of magnesium coated with hydroxyapatite directly synthesized in an aqueous solution. Electrochim Acta 54(27):7085–7093

48. Zoriany MY et al. (2020) Optimized silica-based hybrid coatings for the protection of aluminum against chloride-rich environment. J Sol-Gel Sci Technol 94:257–269

49. Wu X et al. (2013) Crystal structure determination of three polycyclic compounds and comparative Rietveld refinement between MS and GSAS programs. Chin Sci Bull 58(20):2430–2434

50. Altomare A et al. (2015) QUALX2. 0: a qualitative phase analysis software using the freely available database POW_COD. J Appl Crystallogr 48(2):598–603

51. Vaitkus A, Merkys A, Gražulis S (2021) Validation of the crystallography open database using the crystallographic information framework. J Appl Crystallogr 54(2):661–672

52. Gražulis S et al. (2009) Crystallography Open Database–an open-access collection of crystal structures. J Appl Crystallogr 42(4):726–729

53. Renaudin G, Gomes S, Nedelec J-M (2017) First-row transition metal doping in calcium phosphate bioceramics: A detailed crystallographic study. Materials 10(1):92

54. Pai Z et al. (2005) Catalytic oxidation of olefins and alcohols with hydrogen peroxide in a two-phase system giving mono-and dicarboxylic acids. Russian Chem Bull 54:1847–1854

55. Antony C et al. (2011) FT-IR and FT-Raman study of Nasicon type phosphates, ASnFe (PO4) 3 [a= Na2, Ca, Cd]. Spectrochimica Acta Part A 78(1):415–419

56. Tiwari A et al. (2016) Synthesis, characterization and optical properties of polymer-based ZnS nanocomposites. Luminescence 31(2):428–432

57. Ahmed A et al. (2018) XRD and ATR/FTIR investigations of various montmorillonite clays modified by monocationic and dicationic imidazolium ionic liquids. J Mol Struct 1173:653–664

58. Cecen V et al. (2008) FTIR and SEM analysis of polyester-and epoxy-based composites manufactured by VARTM process. J Appl Polym Sci 108(4):2163–2170

59. De G et al. (1993) FTIR studies of gel to glass conversion in TEOS-fumed silica-derived gels. J Non Crystalline solids 155(3):253–258

60. Ivanković M et al. (2009) Preparation and properties of organic–inorganic hybrids based on poly (methyl methacrylate) and sol–gel polymerized 3-glycidyloxypropyltrimethoxysilane. Polymer 50(12):2544–2550

61. Fedel M (2017) Effect of sol–gel layers obtained from GLYMO/MTES mixtures on the delamination of a cataphoretic paint on AA1050. J Coat Technol Res 14(2):425–435

62. Espanol M et al. (2010) Investigation of the hydroxyapatite obtained as hydrolysis product of α-tricalcium phosphate by transmission electron microscopy. CrystEngComm 12(10):3318–3326

63. Targonska S et al. (2019) A new approach to spectroscopic and structural studies of the nano-sized silicate-substituted hydroxyapatite doped with Eu 3+ ions. Dalton Trans 48(23):8303–8316

64. Zhang L, Zhang J, Liu R (2015) Organic–inorganic hybrid sol–gel coatings for corrosion protection of aluminum alloys. Surf Innov 4(2):51–69

65. Kasten L et al. (2001) An XPS study of cerium dopants in sol–gel coatings for aluminum 2024-T3. Surf Coat Technol 140(1):11–15

66. Chambers BD, Taylor SR (2007) The high throughput assessment of aluminium alloy corrosion using fluorometric methods.

Part II – A combinatorial study of corrosion inhibitors and synergistic combinations. Corros Sci 49(3):1597–1609

67. Lopez-Garrity OA (2013) Corrosion inhibition mechanisms of aluminum alloy 2024-T3 by selected non-chromate inhibitors. The Ohio State University, Ann Arbor, p 272

68. Buchheit RG et al. (1997) Local dissolution phenomena associated with S phase (Al2CuMg) particles in aluminum alloy 2024-T3. J Electrochem Soc 144(8):2621–2628

69. Yasakau KA et al. (2006) Mechanism of corrosion inhibition of AA2024 by rare-earth compounds. J Phys Chem B 110(11):5515–5528

70. Chen GS, Gao M, Wei RP (1996) Microconstituent-induced pitting corrosion in aluminum alloy 2024-T3. Corrosion 52(1):8–15

71. Ho D et al. (2006) Cerium dibutylphosphate as a corrosion inhibitor for AA2024-T3 aluminum alloys. J Electrochem Soc 153(9):B392

72. Akid R, Gobara M, Wang H (2011) Corrosion protection performance of novel hybrid polyaniline/sol–gel coatings on an aluminium 2024 alloy in neutral, alkaline and acidic solutions. Electrochim Acta 56(5):2483–2492

73. Rosero-Navarro NC et al. (2009) Improved corrosion resistance of AA2024 alloys through hybrid organic–inorganic sol–gel coatings produced from sols with controlled polymerisation. Surf Coat Technol 203(13):1897–1903

74. Lakshmi R, Sampath S, Aruna S (2021) Silica-alumina based sol-gel coating containing cerium oxide nanofibers as a potent alternative to conversion coating for AA2024 alloy. Surf Coat Technol 411:127007

75. Gobara M et al. (2015) Corrosion behaviour of AA2024 coated with an acid-soluble collagen/hybrid silica sol–gel matrix. Prog Org Coat 89:57–66

76. Zhou Z et al. (2022) Crosslinking control of hydrophobic benzoxazine-based hybrid sol-gel coating for corrosion protection on aluminum alloys. Prog Org Coat 171:107059

77. Kesmez Ö (2020) Hydrophobic, organic–inorganic hybrid sol–gel coatings containing boehmite nanoparticles for metal corrosion protection. Chem Pap 74(2):673–688

78. Sarmento V et al. (2010) Corrosion protection of stainless steel by polysiloxane hybrid coatings prepared using the sol–gel process. Surf Coat Technol 204(16-17):2689–2701

79. Gnedenkov S et al. (2018) Composite coatings formed on the PEO-layers with the use of solutions of tetrafluoroethylene telomers. Surf Coat Technol 346:53–62

80. Lei Q et al. (2020) Sol-gel-based advanced porous silica materials for biomedical applications. Adv Funct Mater 30(41):1909539

81. Miecznikowski K, Cox JA (2020) Electroanalysis based on stand-alone matrices and electrode-modifying films with silica sol-gel frameworks: a review. J Solid State Electrochem 24(11):2617–2631

82. Akbarzadeh S, Paint Y, Olivier M-G (2023) A comparative study of different sol-gel coatings for sealing the plasma electrolytic oxidation (PEO) layer on AA2024 alloy. Electrochim Acta 443:141930

83. Gobara M et al. (2020) Corrosion protection mechanism of Ce4+/organic inhibitor for AA2024 in 3.5% NaCl. RSC Adv 10(4):2227–2240

84. Qi J, Li W (2022) Chromium-based conversion coatings. In Conversion coatings for magnesium and its alloys. Springer, pp 49–71

85. Stoica A-I et al. (2019) Influence of post-treatment time of trivalent chromium protection coating on aluminium alloy 2024-T3 on improved corrosion resistance. Surf Coat Technol 369:186–197

86. Li L, Kim DY, Swain GM (2012) Transient formation of chromate in trivalent chromium process (TCP) coatings on AA2024 as probed by Raman spectroscopy. J Electrochem Soc 159(8):C326

87. Cieplik F et al. (2020) Ca2+ release and buffering effects of synthetic hydroxyapatite following bacterial acid challenge. BMC Oral Health 20(1):1–8

88. Zhang Y, Wang Y (2012) The effect of hydroxyapatite presence on the degree of conversion and polymerization rate in a model self-etching adhesive. Dent Mater 28(3):237–244

89. Wang H, Akid R (2007) A room temperature cured sol–gel anticorrosion pre-treatment for Al 2024-T3 alloys. Corros Sci 49(12):4491–4503

90. Wang H, Akid R, Gobara M (2010) Scratch-resistant anticorrosion sol–gel coating for the protection of AZ31 magnesium alloy via a low temperature sol–gel route. Corros Sci 52(8):2565–2570

91. Chowdhury ND, Ghosh K (2018) Electrochemical behaviour of dental amalgam in natural, artificial saliva and in 0.90 wt.% NaCl solution. Corros Sci 133:217–230

92. Yang H-Q et al. (2021) Effects of immersion temperature on the performance of a marine epoxy-based organic coating for ballast tanks. J Mater Eng Perform 30(6):4458–4465

93. Fan C et al. (2021) Electrochemical behavior and interfacial delamination of a polymer-coated galvanized steel system in acid media. ACS omega 6(31):20331–20340

94. Trevisanello E et al. (2021) Polycrystalline and single crystalline NCM cathode materials—quantifying particle cracking, active surface area, and lithium diffusion. Adv Energy Mater 11(18):2003400

95. Shao Z et al. (2022) High-pressure induced acceleration pathways for water diffusion in heavy duty anticorrosion coatings under deep ocean environment:(I) the samples subjected to high-pressure pre-processing. Prog Org Coat 170:106948

96. Li S et al. (2021) Reinforced anticorrosion performance of waterborne epoxy coating with eco-friendly L-cysteine modified Ti3C2Tx MXene nanosheets. Prog Org Coat 161:106478

97. Ralston KD et al. (2008) Corrosion inhibition of aluminum alloy 2024-T3 by aqueous vanadium species. J Electrochem Soc 155(7):C350

98. Iannuzzi M, Frankel GS (2007) Mechanisms of corrosion inhibition of AA2024-T3 by vanadates. Corros Sci 49(5):2371–2391

99. Zheng T et al. (2021) Corrosion inhibition of AA2024-T3 in alkaline solution by disodium-N-dodecyliminodiacetate: Experimental and theoretical studies. Colloids Surf A: Physicochemical Eng Asp 626:126989

100. Li C, Guo X, Frankel GS (2021) Corrosion inhibition of AA2024-T3 by a coating containing dual-pH sensitive, corrosion inhibitor loaded microspheres. Corros Sci 192:109835